EI SEVIER

Contents lists available at ScienceDirect

# Scripta Materialia

journal homepage: www.elsevier.com/locate/scriptamat



Viewpoint article

# Thermo-mechanical behavior of organic-inorganic halide perovskites for solar cells



Cristina Ramirez, Srinivas K. Yadavalli, Hector F. Garces, Yuanyuan Zhou, Nitin P. Padture \*

School of Engineering, Brown University, Providence, RI 02912, USA

#### ARTICLE INFO

Article history: Received 24 December 2017 Accepted 16 February 2018 Available online 20 March 2018

Keywords: Perovskites Solar cells Mechanical properties Residual stress Residual strain

#### ABSTRACT

Organic-inorganic halide perovskites (OIHPs) are a remarkable family of hybrid materials at the heart of the emerging thin-film perovskite solar cells (PSCs) technology and other applications. In this Viewpoint article, in addition to some original experimental results, thermo-mechanical analyses of residual macro- and micro-stresses in OIHP thin films are presented in the context of fracture of both the OIHP layer itself and its interface with the substrate. The implications of mechanical behavior of OIHPs and interfaces on the reliability of PSCs, as well as opportunities for future research directions in this general area, are highlighted.

© 2018 Acta Materialia Inc. Published by Elsevier Ltd. All rights reserved.

Organic-inorganic halide perovskites (OIHPs) are a fascinating family of hybrid materials that defy classical classification (metals, ceramics, polymers) and fall into the hitherto uncharted territory between conventional 'soft' and 'hard' materials [1]. In the general OIHP formula ABX<sub>3</sub>, typically A is an organic cation, methylammonium (CH<sub>3</sub>NH<sub>3</sub><sup>+</sup> or  $MA^+$ ) or formamidinium (HC(NH<sub>2</sub>)<sub>2</sub><sup>+</sup> or FA<sup>+</sup>); B is Pb<sup>2+</sup>, or Sn<sup>2+</sup>; and X is Cl $^-$ , Br $^-$ , or I $^-$  (Fig. 1A), and their alloy combinations [2,3]. Although OIHPs were discovered in 1978, and their structural understanding, solution-processing, and properties were further developed in the 1990s [2], they did not find widespread interest until the first reported use of OIHP in thin-film solar cells in 2009 [4]. Since then, enormous amount of research has been devoted to OIHPs and perovskite solar cells (PSCs) worldwide [5–10], and now the record efficiency of laboratoryscale PSC stands at 22.7% [11], rivalling that of commercial Si-based solar cells. The promise of low-cost solution-processed, high-efficiency PSCs, and its potential impact on the global renewable energy landscape, is driving this effort worldwide. Furthermore, it is being discovered that OIHPs possess unique and unprecedented (opto)electronic properties, making them useful in other potential applications [12], such as light-emitting diodes [13], lasers [14], and detectors (photon [15], X-ray [16], nuclear-radiation [17], gas [18]).

The crystal structure of OIHPs (Fig. 1A) is based on inorganic framework resulting from the strong B-X ionic/covalent interactions, whereas the A-X bonding is relatively weak. This inorganic-based framework of the OIHP structure is responsible for OIHPs having microstructures (Fig. 1B) typical of 'hard' materials [1,19]. Fig. 1C is a transmission electron microscope (TEM) image showing MAPbl<sub>3</sub> grains and grain boundaries, and

E-mail address: nitin\_padture@brown.edu (N.P. Padture).

also a proliferation of defects within the grains [20]. The latter is due to the intrinsic low formation-energy of the defects in OIHPs [20]. These defects, as well as the ultrafast organic-cation rotation dynamics and ion mobility, are responsible for the 'soft' nature of OIHPs [21]. While their 'soft' nature allows them to access the vast, rich field of organic/inorganic chemistry [12,21], the similarity of their microstructures to 'hard' materials provides rich opportunities to discover new materials science of OIHPs [1].

While new OIHP materials, synthesis/processing, and PSC architectures continue to be popular research topics, the research focus has been shifting towards topics such as large-area PSCs, scalable manufacturing, stability, durability, and reliability, which is essential if PSCs are to be deployed commercially in the future [10]. Since PSCs are made of multiple functional layers of a diverse set of materials with vastly different thermal and mechanical properties. PSCs reliability will depend on the thermo-mechanical behavior of the multilayer stacks that are expected to cycle through thermal excursions during manufacturing and service. Also, PSCs will be subjected to externally applied stresses. While interfacial adhesive fracture is an important issue in multilayer PSCs, it has been shown that the brittle OIHP layer itself is quite often the 'weakest link' where cohesive fracture occurs [22,23]. Despite the rising importance of fracture of OIHPs, as it may ultimately control the reliability of PSCs (Fig. 2) [23], research in this area has been extremely scant [22–24].

## Mechanical and Thermal Properties of MAPbI3 OIHP

The mechanical properties (elastic modulus (E) and hardness (H)) and the linear coefficients of thermal expansion (CTEs  $(\alpha)$ ) of MAPbI<sub>3</sub>, the most widely studied OIHP, have been reported, and are summarized in Tables 1 and 2, respectively. Within these limited experimental data

<sup>\*</sup> Corresponding author.

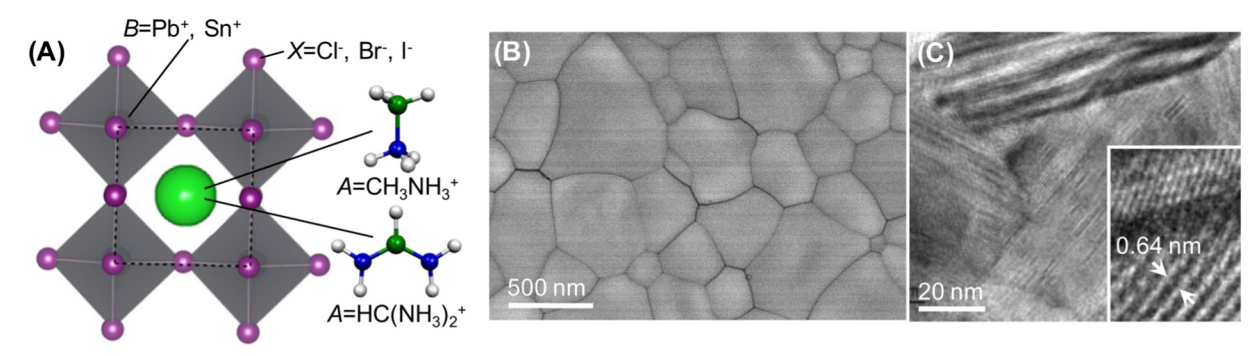


Fig. 1. (A) Schematic illustration of OIHP crystal structure. MAPbl<sub>3</sub> thin film microstructure: (B) SEM image [19] and (C) TEM image showing grain boundaries and defective grains (inset: high-solution TEM image) [20]. (Adapted with permission from RSC.)

there appears to be some variation. With regards to E and H properties, all the studies on MAPbI $_3$  are based on the indentation technique [23,25–29], which is highly sensitive to the surface conditions. Also, the E and H measurements depend on the indentation dwell time as MAPbI $_3$  creeps significantly at room temperature at dwell times as short as 20 s [28]. In the case of CTEs, the origin of the variation could be due to the nature of the samples studied: single-crystals [30], films [31], and powders [32,33]. Nevertheless, the measured CTEs of MAPbI $_3$  are significantly higher than that of soda-lime silicate glass ( $\alpha_{Glass} \sim 10 \times 10^{-6} \, ^{\circ} C^{-1}$ ) [34], which is commonly used as the substrate material in PSCs.

Here we have measured *E* and *H* values of a carefully prepared MAPbI<sub>3</sub> single-crystal (100 face) using the nanoindentation technique, and they are reported in Table 1 (see Supplementary Information (SI) for experimental details). A Berkovich diamond indenter was used, and the dwell time at peak load was limited to 0.5 s in order to preclude any creep effects [28]. An average *E* value of 17.8 GPa is obtained using the Oliver and Pharr analysis [35], which is on the high side compared to that reported in the literature (Table 1). At 20-s dwell time, the average *E* value drops to 12.7 GPa, which is in the ballpark of what others have reported (Table 1). Similarly, the average *H* values are 0.58 GPa and 0.48 GPa at 0.5 s and 20 s dwell time, respectively. While most papers do not report indentation dwell time, from the reported load-displacement curves it appears that most studies use dwell times approaching

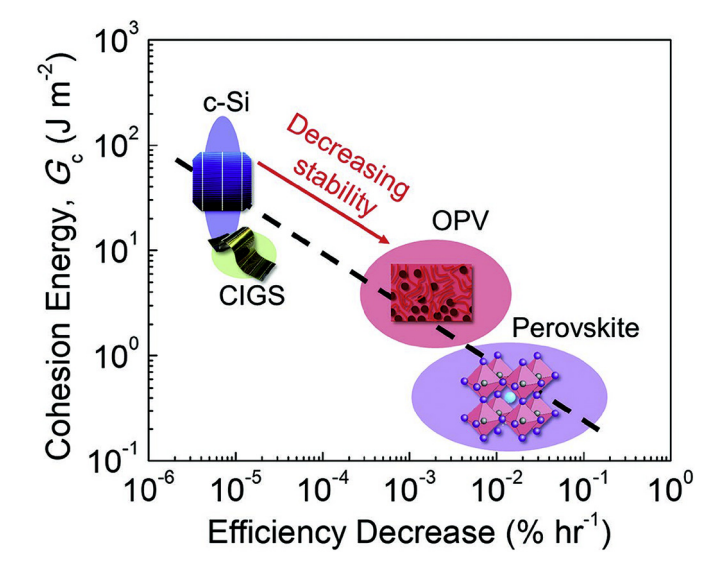


Fig. 2. The measured cohesion,  $G_{\mathbb{C}}$  (same as  $\Gamma_0$ ), and degradation rate as a function of solar cell active material, showing a correlation between mechanical integrity and long-term reliability [23].

(Adapted with permission from VCH-Wiley.)

 $20 \, \mathrm{s}$  or longer. Our results clearly show that room-temperature indentation creep is important, and, thus, it is recommended that very short dwell time (0.5 s) be used in future indentation experiments to preclude any creep effects that can result in the erroneous underestimation of E and H.

The cohesive fracture energy ( $\Gamma_{\rm O}$ ) of polycrystalline MAPbI<sub>3</sub> thin films has been reported to be in the range 0.24–1.48 J·m<sup>-2</sup> (Table 3), as measured using the double-cantilever-beam delamination test [22,23]. Using *E* of 17.8 GPa, this translates to a toughness ( $K_{\rm IC}$ ) range of 0.06–0.16 MPa·m<sup>0.5</sup>, where  $K_{\rm IC} = (\Gamma_{\rm O}E)^{0.5}$  [36]. While these values are comparable to single-crystal NaCl salt (0.15–0.26 MPa·m<sup>0.5</sup> [22]), they are quite low compared to other brittle inorganic materials used in solar cells such as silicon and glass ( $K_{\rm IC} \sim 0.7$  MPa·m<sup>0.5</sup>) [36]. In this context, we have used nanoindentation to estimate the  $K_{\rm IC}$  values of single-crystal MAPbI<sub>3</sub> OIHP (100 face). A cube-corner diamond indenter is used in order to promote crack formation at a low nanoindentation load (P), and it is aligned to result in cracking along the easy-cleavage plane. The crack size, c, is measured and the  $K_{\rm IC}$  is estimated using the following equation: [37]

$$K_{\rm IC} = \alpha \left(\frac{E}{H}\right)^{0.5} \frac{P}{c^{1.5}},\tag{1}$$

where the constant  $\alpha$  is given by  $\{(0.0352/(1-\nu)\} \times (\cot\Psi)^{0.67}$ . The included angle  $\Psi$  for cube-corner indenter is 35.3°, which is much sharper than that for the Berkovich indenter ( $\Psi=65.3^{\circ}$ ), and  $\nu$  is the Poisson's ratio (=0.33) [25]. Using E/H=30.7 (Table 1), the average  $K_{\rm IC}$  is estimated at 0.22 MPa·m<sup>0.5</sup>. Note that a longer dwell time (20 s) results in an erroneous underestimation of the  $K_{\rm IC}$  (Table 3). Recently, Rolston et al. [23] have reported a  $K_{\rm IC}$  of 0.15 MPa·m<sup>0.5</sup> for single-crystal MAPbl<sub>3</sub> OIHP using the Vicker's indentation method (10 s dwell time) [36].

 $\begin{tabular}{ll} \textbf{Table 1} \\ Elastic modulus and hardness values of single-crystal MAPbI_3 measured using indentation techniques. \end{tabular}$ 

E (GPa)	H (GPa)	E/H	Remarks	Ref.
14.3	0.57	25.1	100 face	[25]
14.0	0.55	25.5	112 face	
10.4	0.42	24.8	100 face	[26]
10.7	0.46	23.3	112 face	
20.0	1.0	20.0	-	[27]
10.8	0.55	19.6	100 face	[28]
	0.47		_	[29]
	-	100 <sup>a</sup>		[23]
17.8 <sup>b</sup>	0.58 <sup>b</sup>	30.7 <sup>b</sup>	100 face	This study
12.7 <sup>c</sup>	0.48 <sup>c</sup>	26.5 <sup>c</sup>	100 face	This study

- a Knoop indentation.
- b Dwell time 0.5 s.
- <sup>c</sup> Dwell time 20 s.

**Table 2**Linear CTE values of MAPbI<sub>3</sub> and temperature ranges.

Cubic (°C <sup>−1</sup> )	Tetragonal (°C <sup>-1</sup> )	Pseudocubic (°C <sup>-1</sup> )	Remarks	Ref.
$\alpha_a = 42.4 \times 10^{-6}$ (T: 57 to 87 °C)	-	$\alpha_{AVE} = 44.5 \times 10^{-6} \text{ a}$ (T: -103 to 56 °C)	Single-crystal; CTE extracted	[30]
$\alpha_a = 47.7 \times 10^{-6}$ (T: 54 to 98 °C)	$\alpha_{a,b} = 132 \times 10^{-6}$ $\alpha_c = -106 \times 10^{-6}$ (T: 35 to 51 °C)	$\alpha_{AVE} = 52.3 \times 10^{-6} \text{ a}$ (T: 35 to 53 °C)	Drop-cast film; CTE reported	[31]
$\alpha_a = 35.1 \times 10^{-6}$ (T: 51 to 77 °C)	-	$\alpha_{AVE} = 42.4 \times 10^{-6 \text{ b}}$ (T: $-113 \text{ to } 52 \text{ °C}$ )	Powder; CTE reported	[32,33]

<sup>&</sup>lt;sup>a</sup> Based on volume CTE ( $\alpha_{AVE} = \alpha_{VOL}/3$ ).

Now we are placed to perform analyses of residual macro- and micro-stresses in planar OIHP thin films. Considering the paucity of thermal and mechanical properties data for other OIHPs, these analyses are limited to MAPbl<sub>3</sub> thin films as a case study. The upper-bound CTE values from Table 2 are used to calculate the maximum possible residual stresses as the worst-case scenario.

#### **Macroscopic Residual Stresses**

Most solution-processed MAPbI<sub>3</sub> thin films are typically crystallized at an elevated temperature (T) of 100–150 °C, and are generally deposited on thick glass substrates having a thin coating of a transparent conduction oxide, typically fluorinated tin oxide (FTO) or indium tin oxide (ITO). Thus, during cooling, the polycrystalline MAPbI<sub>3</sub> thin film is in a state of equi-biaxial in-plane residual tensile stress due the CTE mismatch with the substrate (assuming perfect film/substrate bonding), which is described as macro-stress ( $\sigma_{Macro}$ ; Fig. 3). Since the thin-film contraction is not constrained by the substrate in the vertical direction, the out-of-plane strain is only due to the Poisson's effect ( $\nu = 0.33$ ), which is a third of the in-plane strain and of the opposite sign. Thus, the out-of-plane residual stress is expected to be zero. Also, the glass substrate is massive (millimeters) compared to the MAPbI<sub>3</sub> thin film ( $\sim$ 500 nm) and the FTO/ITO coating ( $\sim$ 1  $\mu$ m), and, therefore, the residual stress generated in the glass substrate is negligible. (Note that this may not be the case in thin, low-E flexible polymer substrates, such as polyethylene terephthalate or PET.) Using 150 °C as the upper bound temperature, and 55 °C as the cubic-to-tetragonal transformation temperature [38,39], the maximum residual  $\sigma_{Macro}$  in a cubic polycrystalline MAPbI<sub>3</sub> thin film on glass substrate at 55 °C ( $\Delta T = 150-55 =$ 95 °C) is calculated using the following: [40]

$$\sigma_{\text{Macro}} = E \Delta \alpha \Delta T, \tag{2}$$

where  $\Delta\alpha = (\alpha_a - \alpha_{Glass})(47.7 \times 10^{-6} - 10 \times 10^{-6}) = 37.7 \times 10^{-6} \,^{\circ}\text{C}^{-1}$ . The cubic MAPbl<sub>3</sub> CTE values from Table 2 are used here, but *E* value corresponding to tetragonal MAPbl<sub>3</sub> (100) we measured ( $E = 17.8 \,\text{GPa}$ ) is used, because *E* for cubic MAPbl<sub>3</sub> is unknown but it is unlikely to be very different from that of tetragonal MAPbl<sub>3</sub>. During further cooling of the tetragonal MAPbl<sub>3</sub> thin films from 55 °C to room temperature (25 °C;

**Table 3** Fracture energy and toughness of MAPbI<sub>3</sub> thin films and single-crystals.

$\Gamma_{O}\left(J\!\cdot\!m^{-2}\right)$	$K_{IC}$ (MPa·m <sup>0.5</sup> )	Remarks	Ref.
0.24 1.48	0.06 <sup>a</sup>	Capping-layer on mesoscopic film	[22] [22]
0.83	0.10 a	Slot-die-coated film	[23]
1.26 <sup>a</sup> 2.72 <sup>a,b</sup>	0.15 0.22 <sup>b</sup>	Single-crystal Vicker's indentation Single-crystal (100 face) cube-corner	[23] This study
2.72	0,22	nanoindentation	iiiis study
1.82 <sup>a,c</sup>	0.18 <sup>c</sup>		This study

<sup>&</sup>lt;sup>a</sup> Calculated using E = 17.8 GPa.

 $\Delta T=55-25=30$  °C), additional  $\sigma_{Macro}$  is generated. Assuming that no significant volume change occurs during the cubic-to-tetragonal transformation at 55 °C [31], and that the polycrystalline MAPbI $_3$  thin film has randomly-oriented grains, we use  $\Delta\alpha=(\alpha_{Ave}-\alpha_{Glass})=(52.3\times10^{-6}-10\times10^{-6})=42.3\times10^{-6}$  °C $^{-1}$  in Eq. (2) to calculate that additional  $\sigma_{Macro}$ . Thus, the total  $\sigma_{Macro}$  in a typical non-textured polycrystalline MAPbI $_3$  thin film on a glass substrate at room temperature (cooled from 150 °C) is 86 MPa, corresponding to a maximum biaxial tensile residual strain of 0.49% in the film. If the thin film is cooled down further to -40 °C, the lowest solar-panels test temperature, the total tensile residual  $\sigma_{Macro}$  at -40 °C is 135 MPa. These results are plotted in Fig. 4A as a function of temperature.

The  $\sigma_{\text{Macro}}$  in films can induce spontaneous fracture without the application of external stress if a sufficiently large incipient crack exists in the thin film. The critical radius of a half-penny surface crack,  $c_*$ , (Fig. 3A) can be calculated using: [36]

$$c_* = \pi \left(\frac{K_{\text{IC}}}{2\sigma_{\text{Marro}}}\right)^2. \tag{3}$$

Using the intrinsic toughness of MAPbI<sub>3</sub>,  $K_{\rm IC}=0.22~{\rm MPa\cdot m}^{0.5}$ , and the maximum biaxial tensile residual  $\sigma_{\rm Macro}=135~{\rm MPa}$  (at  $-40~{\rm ^{\circ}C}$ ), the calculated  $c_{\rm ^{\circ}}$  value is 2.1 µm. Since typical MAPbI<sub>3</sub> thin films in PSCs are ~500 nm thick, it is impossible to have an incipient crack deeper than the film thickness. However, using the lower bound  $K_{\rm IC}=0.06~{\rm MPa\cdot m}^{0.5}$  [22] as the worst-case scenario, the calculated  $c_{\rm ^{\circ}}$  is 154 nm; it is possible to have such incipient flaws in a 500-nm thin film. The  $c_{\rm ^{\circ}}$  values corresponding to the maximum possible  $\sigma_{\rm Macro}$  as a function of temperature are plotted in Fig. 4B. The fact that the  $c_{\rm ^{\circ}}$  Curve fall below the dashed line (500 nm) only for the worst-case scenario in terms of upper bound  $\sigma_{\rm Macro}$  and lower bound  $K_{\rm IC}$  indicates that CTE-mismatch-induced spontaneous cracking (i.e. without the application of external stress) in well-made MAPbI<sub>3</sub> OIHP thin films may not be a big concern. However, if incipient cracks do propagate

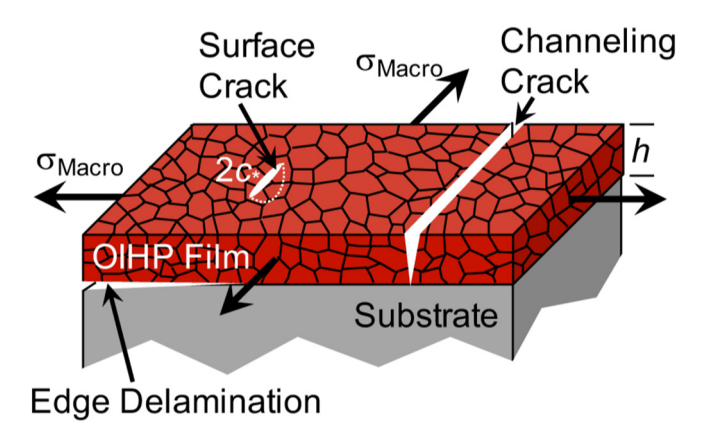


**Fig. 3.** Schematic illustration of polycrystalline (non-textured) OIHP thin film under equibiaxial tensile residual macro-stress ( $\sigma_{\text{Macro}}$ ), with 'half-penny' critical surface crack (diameter  $2c_1$ ), channeling crack (c=h), and edge delamination.

<sup>&</sup>lt;sup>b</sup> Based on tetragonal CTEs ( $\alpha_{AVE} = (2\alpha_a + \alpha_c)/3$ ).

b Dwell time 0.5 s.

<sup>&</sup>lt;sup>c</sup> Dwell time 20 s.

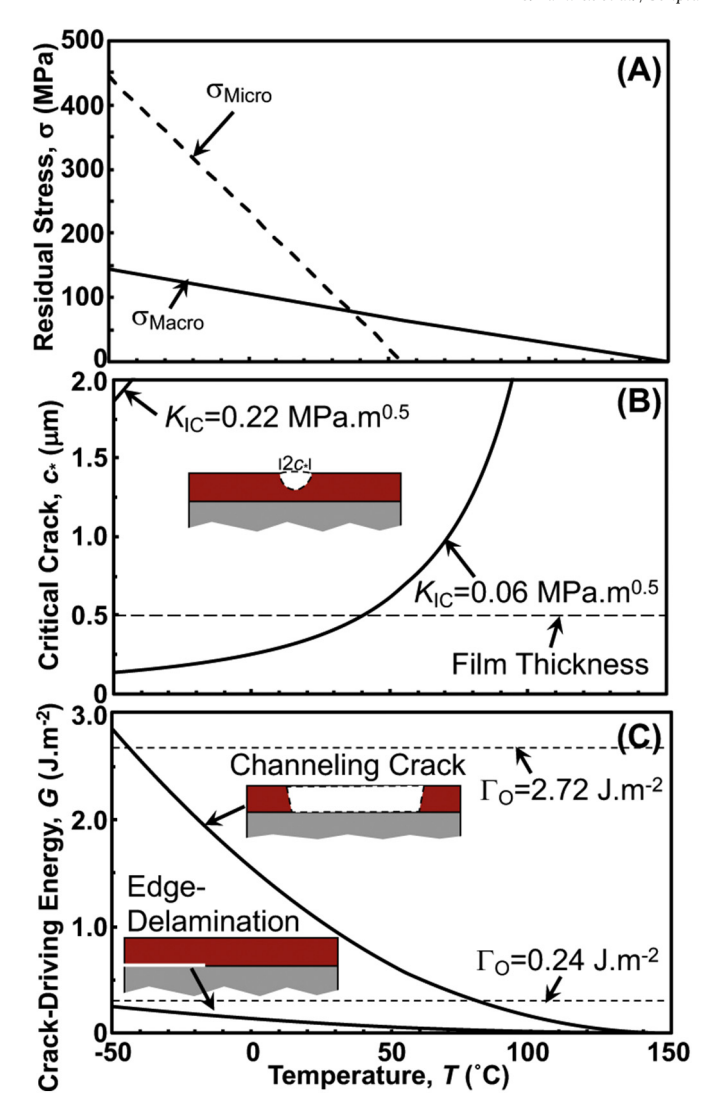


**Fig. 4.** (A) Calculated maximum possible tensile residual  $\sigma_{\text{Macro}}$  and  $\sigma_{\text{Micro}}$  in a non-textured polycrystalline MAPbl<sub>3</sub> thin film as a function of temperature of the film cooled from 150 °C. (B) Calculated 'half-penny' critical surface crack radii (c·) in the above film corresponding to  $\sigma_{\text{Macro}}$  from (A) using upper and lower bound  $K_{\text{IC}}$  values. Dashed horizontal line indicates film thickness of ~500 nm, c- above which have no physical meaning. (C) Calculated crack-driving energy, G, for channeling crack and edge delamination using  $\sigma_{\text{Macro}}$  from (A). Dashed lines in (C) indicate upper and lower bounds  $\Gamma_{\text{O}}$  values.

through-thickness of the film, they will be arrested at the interface because the substrate is significantly tougher. However, they can channel across the film (Fig. 3), the condition for which is given by: [41]

$$G = \frac{c_e^2 \pi h \sigma_{\text{Macro}}^2}{F} \ge \Gamma_0, \tag{4}$$

where G crack-driving energy (strain energy release rate) and  $c_{\rm e}$  is a constant (=1.258). Assuming a film thickness h=500 nm and using  $\sigma_{\rm Macro}$  from Fig. 4A, G as a function of temperature is plotted in Fig. 4C. Since Eq. (5) is satisfied even for upper bound  $\Gamma_{\rm O}$  at low temperatures, through-thickness cracks of radius c=h (propagated from c- or pre-existing in the film) are likely to channel along the film. Note that due to the equi-biaxial nature of the residual stress, multiple chanelling cracks can propagate in different directions creating a 'mudflat' cracking pattern. The residual tensile  $\sigma_{\rm Macro}$  can also induce mode-II edge delamination of the MAPbI<sub>3</sub> thin film from the substrate (Fig. 3), condition for which is given by: [41,42]

$$G = \frac{\left(1 - \nu^2\right) h \sigma_{\text{Macro}}^2}{2E} \ge \Gamma_i, \tag{5}$$

where  $\Gamma_i$  is the interfacial adhesive fracture energy. Assuming a film thickness h=500 nm and using  $\sigma_{\text{Macro}}$  from Fig. 4A, G as a function of temperature is also plotted in Fig. 4C. Since  $\Gamma_i > \Gamma_O$  in most cases, as evinced by the fact that fracture occurs within the MAPbI<sub>3</sub> layer and not at the interface [22,23], and G is below the lower bound  $\Gamma_O$ , interfacial adhesive fracture in unlikely to occur due to  $\sigma_{\text{Macro}}$  in well-adhered MAPbI<sub>3</sub> thin films.

Note that the 150 °C film-formation temperature used in these calculations is on the high side, and some mechanical attachment between the crystallizing film and the substrate may occur at lower temperatures during deposition. Thus, the maximum  $\sigma_{\rm Macro}$  calculated above are likely to be overestimates. Also note that fully-crystalline MAPbI $_{3}$  thin films can be deposited at or near room-temperature using scalable methods such as antisolvent-solvent extraction [43] and gas-induced formation and transformation (GIFT) [21,44], where no further heat-treatment is required. In those cases,  $\sigma_{\rm Macro}$  at room temperature is expected to be zero. For a temperature excursion to -40 °C ( $\Delta T = |-40-25| = 65$  °C), the residual tensile  $\sigma_{\rm Macro}$  is calculated to be 49 MPa.

The anisotropic CTE of tetragonal MAPbI<sub>3</sub> below 55 °C has implications on the  $\sigma_{Macro}$  residual stresses if the films are textured. It has been observed that some solution-processed MAPbI<sub>3</sub> thin films have a 110 "mosaic" texture [21,44,45], which implies that the c-axis of the tetragonal MAPbI<sub>3</sub> grains is parallel to the film/substrate interface while the a/b axes are not. Using  $\Delta\alpha=(\alpha_c-\alpha_{Glass})=(-106\times10^{-6}-10\times10^{-6})=-116\times10^{-6}\,^{\circ}\text{C}^{-1}$ , a compressive biaxial residual  $\sigma_{Macro}$  is calculated to be -62 MPa for  $\Delta T=55-25=30\,^{\circ}\text{C}$ . Thus, the total  $\sigma_{Macro}$  in a typical 110-textured polycrystalline MAPbI<sub>3</sub> thin film at room temperature (cooled from 150 °C) is 2 MPa, which is negligible. Thus, there is a clear advantage in having 110 'mosaic' texture in polycrystalline MAPbI<sub>3</sub> thin films.

In order to determine the  $\sigma_{\text{Macro}}$  experimentally, we fabricated a non-textured MAPbI<sub>3</sub> thin film (~500 nm) on a glass substrate using the 'solvent engineering' method (heat-treated at 150 °C) [46]. The equi-biaxial residual tensile stresses in this film were measured at room temperature using the established and reliable X-ray diffraction (XRD)  $\sin^2 \psi$  method on a high-resolution diffractometer [47]. (See SI for experimental details.) Fig. 5 plots the  $d_{134}$  planar spacing as a function of  $\sin^2 \psi$  for a film in two orthogonal orientations ( $\phi = 0^\circ$  and 90°). The residual stress is calculated using the following: [47]

$$\sigma_{\text{Macro}} = \left(\frac{E}{1 - \nu}\right)_{<124>} \left(\frac{m}{d_0}\right),\tag{6}$$

where m is the slope of the linear fit to the data in Fig. 5 and  $d_0$  is the stress-free  $d_{134}$  spacing, which is estimated using the y-intercept. Since the elastic constants of MAPbI<sub>3</sub> in the  $\langle 134 \rangle$  directions are not known, the average values for E (=17.8 GPa) and  $\nu$  (=0.33) are used, which is a good approximation considering that {134} are high-index planes. The bi-axial residual tensile  $\sigma_{\text{Macro}}$  are found to be 42 MPa and 35 MPa for  $\phi$  = 0° and 90°, respectively, which is quite uniform. These

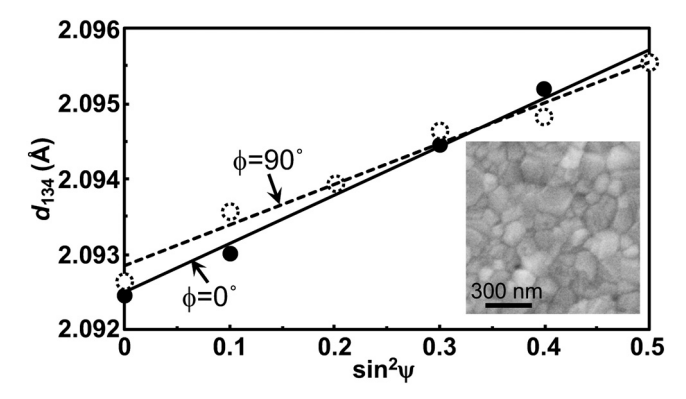


**Fig. 5.** XRD sin<sup>2</sup> $\psi$  plots (at two orthogonal orientations) for MAPbl<sub>3</sub> thin film heat-treated at 150 °C (inset: film top-surface SEM micrograph).

values are rather small (corresponding to ~0.22% average residual tensile strain) and are less than half of the calculated one, but as discussed earlier, the calculated  $\sigma_{\rm Macro}$  is an overestimation. In this context, recently Zhao et al. [48] have used simple peak shifts in XRD patterns of MAPbl<sub>3</sub> thin films (annealed at 100 °C), compared to powder samples, to estimate a CTE-mismatch strain of 0.47%.

#### Microscopic Residual Stresses

The anisotropic CTE will also lead to the generation of localized residual micro-stresses,  $\sigma_{\text{Micro}}$ , at grain boundaries in polycrystalline tetragonal MAPbI<sub>3</sub> thin films as they are cooled from 55 °C to room temperature and below. This is in addition to the overall  $\sigma_{Macro}$ , which will be superimposed on the local  $\sigma_{\text{Micro}}$ . At this juncture, it is instructive to discuss the nature of the cubic-to-tetragonal transformation in MAPbI<sub>3</sub>. This phase transformation is displacive (diffusionless), involving cooperative tilting of the PbI<sub>6</sub> octahedra around 001 (one-tilt system,  $a^0a^0c^-$  in Glazer notation) with respect to the parent cubic phase (Fig. 6A) [30]. Now consider a polycrystalline MAPbI<sub>3</sub> OIHP thin film in the cubic phase just above 55 °C with randomly-oriented grains (Fig. 6B). The  $\sigma_{\text{Micro}}$  is zero at any grain boundary since the CTE (a second rank tensor) of the cubic phase is isotropic (Fig. 6B). Assuming that the entirety of each cubic grain transforms to a corresponding tetragonal grain, the tetragonal unit cell can form with its c-axis aligned along any of the three axes of its parent cubic phase. Thus, the tetragonal grain can have six possible crystallographically-equivalent orientations with respect to its parent cubic grain, making it a ferroelastic material by definition [49]. Upon further cooling, although the unit-cell volumecontraction is similar to the cubic unit cell,  $\sigma_{Micro}$  will start to build up at the grain boundaries between adjacent grains due to the CTE anisotropy (Fig. 6B). (Note that in a non-textured polycrystalline material all the individual  $\sigma_{\text{Micro}}$  will add up to zero overall [40].) The magnitude of  $\sigma_{Micro}$  at individual grain boundaries will depend on the misorientation between the adjacent grains. The best-case scenario is when the caxes of adjacent grains are aligned, where  $\sigma_{\!\scriptscriptstyle Micro}$  is expected to be zero. The worst-case scenario is when the *c*-axis of a grain is aligned with the a/b axis of the neighboring grain (Fig. 5B). In that case,  $\Delta \alpha = (\alpha_c - \alpha_a)$  $_{b}$ ) =  $|(-106 \times 10^{-6} - 132 \times 10^{-6})| = 238 \times 10^{-6} \, ^{\circ}\text{C}^{-1}$ , and using  $\Delta T =$ (55-25) = 30 °C,  $\sigma_{Micro}$  at room temperature is calculated to be 127 MPa. In the case of cooling to -40 °C, the  $\sigma_{\text{Micro}}$  is calculated to be

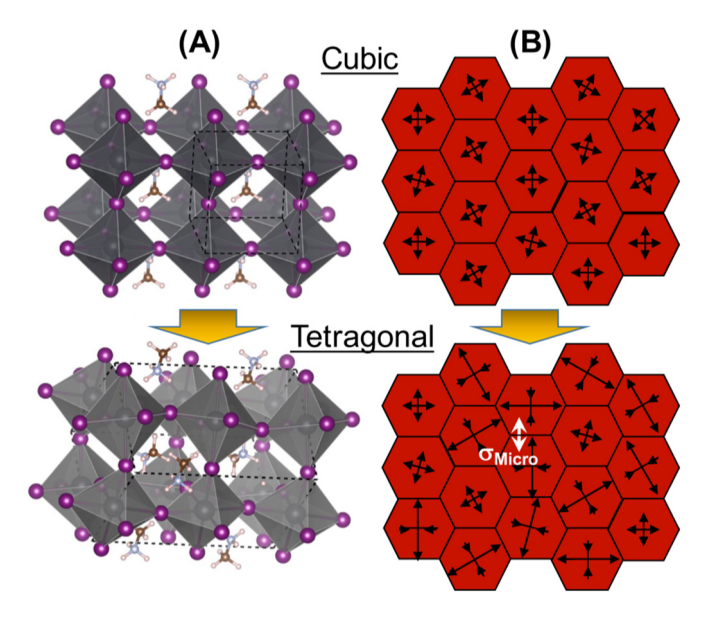


**Fig. 6.** Schematic illustrations of: (A) the cubic-tetragonal transformation in a perovskite and (B) a polycrystalline (not textured) microstructure showing isotropic CTE in cubic phase (top) and anisotropic CTE in the tetragonal phase (bottom) perovskite. Arrows in (B) not to scale.

403 MPa, which is significant. The  $\sigma_{\text{Micro}}$  will superimpose on  $\sigma_{\text{Macro}}$  (Fig. 4A), but  $\sigma_{\text{Micro}}$  alone can induce grain-boundary microcracks in the film, where critical grain-boundary flaws will propagate, however, they will arrest as they run into compression at neighboring grain-boundaries [40]. However, although a large maximum  $\sigma_{\text{Micro}}$  is calculated in non-textured MAPbI $_{3}$  thin films above, it is unlikely to be sustained. This is because  $\sigma_{\text{Micro}}$  can force the formation of the different orientational variants (ferroelastic domains) within individual grains in order to accommodate the CTE-anisotropy-induced residual strain, thereby reducing the maximum  $\sigma_{\text{Micro}}$ . Thus, microcracking is also unlikely to be a major issue in MAPbI $_{3}$  thin films. (Note that grain-boundary cracks are often seen in SEM images of MAPbI $_{3}$  films in the literature (e.g. Fig. 1B), but they are typically induced by the electron-beam during the SEM observation, and, therefore, are an artifact [50].)

The domains formation in the form of intersecting 'stripes' is the hallmark of ferroelastic materials [49], and unsurprisingly it has been observed in MAPbI<sub>3</sub> thin films [51–53], and also in single-crystals [53]. While all the ferroelastic domains are crystallographically equivalent and have the same energy, they can be switched by applying mechanical stress, again, a unique property of ferroelastic materials. Since ferroelastic materials exhibit stress-strain hysteresis, there is a minimum required stress to switch the domains — the coercive stress. This raises the intriguing possibility of toughening MAPbI<sub>3</sub> using ferroelastic switching. Reversible ferroelastic toughening has been established in some ceramics [54], with the most prominent example being Y<sub>2</sub>O<sub>3</sub>-stabilized ZrO<sub>2</sub> used in thermal barrier coatings for jet-engine components [55]. Here, the stress field ahead of the crack tip causes ferroelastic-domain switching, thereby absorbing the applied mechanical energy that would have otherwise gone into crack propagation, i.e. toughening. However, if the coercive stress threshold is not reached in the crack-tip stress field, then toughening will not occur. In general, higher intrinsic fracture resistance ( $\Gamma_0$ ) results in higher stresses in the crack-tip field, triggering ferroelastic toughening:  $\Gamma = \Gamma_0(1 + \Gamma_{FE})$ , where  $\Gamma$  is the total steady-state fracture resistance and  $\Gamma_{FE}$  is the contribution from ferroelastic toughening. Unfortunately, the intrinsic  $\Gamma_0$  of MAPbI<sub>3</sub> is low (~2.7 J·m<sup>-2</sup> (Table 1), compared with  $\sim 6 \, \text{J} \cdot \text{m}^{-2}$  for YSZ ceramic [36],) and, therefore, it remains to be seen if there is a window of stress states where MAPbI<sub>3</sub> can be ferroelastically toughened. In this context, other toughening approaches are being pursued. For example, infiltrating MAPbI<sub>3</sub>-based OIHP into porous oxides/ carbon results in an unprecedented  $\Gamma_0$  in excess of 3 J·m<sup>-2</sup>, which is attributed to the composite-like structure that shields the OIHP from the mechanical loads [23]. Of course, as the OIHP layers are toughened, fracture will occur in the next weakest layer or interface [22].

#### **Other Considerations**

Similar analyses can be performed on other OIHPs such as  $\alpha\text{-FAPbI}_3$  and its alloys. The  $\alpha\text{-FAPbI}_3$  phase, which has a more desirable band gap compared to MAPbI $_3$  for single-junction solar cells, is cubic [56]. Thus,  $\alpha\text{-FAPbI}_3\text{-based}$  thin films will not have residual micro-stresses  $(\sigma_{\text{Micro}})$  and ferroelasticity. The mechanical [57] and CTE [58,59] properties needed for the thermo-mechanical analyses of these materials have become available, and they appear to be quite similar to those of MAPbI $_3$ . Most recently,  $\Gamma_O$  values for various (MA,FA,Cs)PbI $_3$  alloy OIHP thin films have been measured, but they appear to be rather low (0.25–0.59 J·m $^{-2}$ ) [23].

The thermomechanical analyses so far have been linear elastic. OIHPs will deform plastically when the residual shear stress exceeds the yield strength  $(\tau_Y)$ , which is estimated at 370 MPa for single-crystal MAPbI $_3$  [28]. The maximum residual shear stress in a thin film with the maximum estimated biaxial tensile stress of  $\sigma_{Macro}=135$  MPa is  $\tau_{Max}=\sigma_{Macro}/2=67.5$  MPa, which is much smaller than the  $\tau_Y$ . Thus,  $\sigma_{Macro}$  is unlikely to induce plastic deformation of MAPbI $_3$  thin films.

While the above analyses are performed only for CTE-mismatch/anisotropy-induced residual stresses and spontaneous cracking/delamination, they can be extended to situations where additional applied

stresses ( $\sigma_{App}$ ) are superimposed. The  $\sigma_{App}$  on the OIHP thin films and interfaces can result from flexing, peeling, constraint, *etc.* during manufacturing, device-packaging, handling, and in-service. The  $\sigma_{App}$  may be more severe compared to residual  $\sigma_{Macro}$  and  $\sigma_{Micro}$ , which can cause serious fracture damage and attendant degradation of the devices. For example, most recently it has been shown that the use of a stiff PSCs encapsulation material, which provides added constraint, is more detrimental to the thermal-cycling performance of the PSCs compared to when a more compliant encapsulation material is used [60].

#### Outlook

In closing, this Viewpoint article has only scratched the surface regarding the thermo-mechanical behavior of OIHP thin films. If past experience in achieving unprecedented reliability in commercial wafer and thin-film multilayer solar cells is any guide, the reliability of the multilayer PSCs will become critically important as they are poised for commercial deployment. This will make further studies of, not only thermo-mechanical behavior of OIHPs themselves, but also the whole PSC multilayer, indispensable. This presents rich opportunities for future experimental and computational research in topics including, but not limited to: (1) mechanical properties (elastic, plastic, fracture, toughening, creep, fatigue) of OIHPs and interfaces; (2) environmental effects on mechanical properties of OIHPs and interfaces; (3) OIHP thermal properties (expansion, conductivity); (4) in situ characterization of residual and applied stresses/strains, and deformation/failure; (5) OIHP microstructural effects (grain size, texture, grain-boundary engineering); (6) OIHP composition/phase/structural-dimensionality effects; (7) chemo-mechanical effects (diffusion, degradation, synthesis/processing); (8) photo-mechanical effects; (9) thermo-mechanical behavior of interfaces in multilayers; and (10) overall device reliability.

#### Acknowledgements

This research is supported by the Office of Naval Research (N00014-17-1-2232) and the National Science Foundation (OIA-1538893). Experimental assistance from Dr. Y. Lu in performing the nanoindentation tests is gratefully acknowledged.

# Appendix A. Supplementary information

Supplementary information to this article can be found online at https://doi.org/10.1016/j.scriptamat.2018.02.022.

### References

- [1] Y. Zhou, O.S. Game, S. Pang, N.P. Padture, J. Phys. Chem. Lett. 6 (2015) 4827–4839.
- [2] D.B. Mitzi, in: K.D. Karlin (Ed.), Progress in, John Wiley & Sons, Inorganic Chemistry, New York, NY, 1999.
- [3] B. Saparov, D.B. Mitzi, Chem. Rev. 116 (2016) 4558–4596.
- [4] A. Kojima, K. Teshima, Y. Shirai, T. Miyasaka, J. Am. Chem. Soc. 131 (2009) 6050–6051.
- [5] H.-S. Kim, C.-R. Lee, J.-H. Im, K.-B. Lee, T. Moehl, A. Marchioro, S.-J. Moon, R. Humphrey-Baker, J.-H. Yum, J.E. Moser, M. Grätzel, N.-G. Park, Sci. Rep. 2 (2012) 591.
- [6] M.M. Lee, J. Teuscher, T. Miyasaka, T.N. Murakami, H.J. Snaith, Science 338 (2012) 643–647.
- [7] M. Liu, M.B. Johnston, H.J. Snaith, Nature 501 (2013) 395–398.
- [8] J.H. Heo, S.H. Im, J.H. Noh, T.N. Mandal, C.-S. Lim, J.A. Chang, Y.H. Lee, H.-J. Kim, A. Sarkar, M.K. Nazeeruddin, M. Grätzel, S.I. Seok, Nat. Photonics 7 (2013) 486–491.
   [9] N.-G. Park, M. Grätzel, T. Miyasaka, Organic-inorganic Halide Perovskite Photovoltaics:
- From Fundamentals to Device Architectures, Springer, Zurich, Switzerland, 2016.
- [10] J.-P. Correa-Baena, M. Saliba, T. Buonassisi, M. Grätzel, A. Abate, W. Tress, A. Hagfeldt, Science 358 (2017) 739–744.
- [11] NREL, www.nrel.gov/ncpv/images/efficiency\_chart.jpg 2017.
- [12] Y. Zhao, K. Zhu, Chem. Soc. Rev. 45 (2016) 655689
- [13] Z.-K. Tan, R.S. Moghaddam, M.L. Lai, P. Docampo, R. Higler, F. Deschler, M. Price, A. Sadhanaia, L.M. Pazos, D. Credgington, F. Hanusch, T. Bein, H.J. Snaith, R.H. Friend, Nat. Nanotechnol. 9 (2014) 687–692.
- [14] G. Xing, N. Matthews, S.S. Lim, N. Yantara, X. Liu, D. Sabba, M. Grätzel, S. Mhaisalkar, T.C. Sum, Nat. Mater. 13 (2014) 476–480.
- [15] L. Dou, Y. Yang, J. You, Z. Hong, W.-H. Chang, G. Li, Y. Yang, Nat. Commun. 5 (2014) 5404.

- [16] S. Yakunin, M. Sytnyk, D. Kriegner, S. Shrestha, M. Richter, G.J. Matt, H. Azimi, C. Braher, J. Stang, M.V. Koyalenko, W. Heiss, Nat. Photonics, 9 (2015) 444–449.
- [17] Q. Dong, Y. Fang, Y. Shao, P. Mulligan, J. Qiu, L. Cao, J. Huang, Science 347 (2015) 967–970.
- [18] C. Bao, J. Yang, W. Zhu, X. Zhou, H. Gao, F.M. Li, G. Fu, T. Yu, Z. Zou, Chem. Commun. 51 (2015) 15426–15429.
- [19] H. Hu, D. Wang, Y. Zhou, J. Zhang, S. Lv, S. Pang, X. Chen, Z. Liu, N.P. Padture, G. Cui, RSC Adv. 4 (2014) 28964–28967.
- [20] Y. Zhou, M. Yang, A.L. Vasiliev, H.F. Garces, Y. Zhao, D. Wang, S. Pang, K. Zhu, N.P. Padture, I. Mater. Chem. A 3 (2015) 9249–9256.
- [21] Y. Zhou, N.P. Padture, ACS Energy Lett. 2 (2017) 2166–2176.
- 22] N. Rolston, B.L. Watson, C.D. Bailie, M.D. McGehee, J.P. Bastos, R. Gehlhaar, J.-E. Kim, D. Vak, A.T. Mallajosyula, G. Gupta, A.D. Mohite, R.H. Dauskardt, Extreme Mech. Lett. 9 (2016) 353–358.
- [23] N. Rolston, A.D. Printz, J.M. Tracy, H.C. Weerasinghe, D. Vak, L.J. Haur, A. Priyadarshi, N. Mathews, D.J. Slotcavage, M.D. McGehee, R.E. Kalan, K. Zielinski, R.L. Grimm, H. Tsai, W. Nie, A.D. Mohite, S. Gholipour, M. Saliba, M. Grätzel, R.H. Dauskardt, Adv. Energy Mater. (2018) (in press) https://doi.org/10.1002/aenm.201702116.
- [24] J.-H. Kim, I. Lee, T.-S. Kim, N. Rolston, B.L. Watson, R.H. Dauskardt, MRS Bull. 42 (2017) 115–123
- 25] Y. Rakita, S.R. Cohen, N.K. Kedem, G. Hodes, D. Cahen, MRS Commun. (2015) 1–7.
- [26] S. Sun, Y. Fang, G. Kieslich, T.J. White, A.K. Cheetham, J. Mater. Chem. A 3 (2015) 18450–18455
- [27] M. Spina, A. Karimi, W. Andreoni, C.A. Pignedoli, B. Nafradi, L. Forro, E. Horvath, Appl. Phys. Lett. 110 (2017), 121903.
- [28] M.A. Reyes-Martinez, A.L. Abdelhady, M.I. Saidaminov, D.Y. Chung, O.K. Bakr, M.G. Kanatzidis, W.O. Soboyejo, Y.-L. Loo, Adv. Mater. 29 (2017), 1606556.
- [29] S. Shreshtha, R. Fischer, G.J. Matt, P. Feldner, T. Michel, A. Osvert, I. Levchuk, B. Merle, S. Golkar, H. Chen, S.F. Tedde, O. Schmidt, R. Hock, M. Ruehrig, M. Goeken, W. Heiss, G. Anton, C.J. Brabec, Nat. Photonics 11 (2017) 436–440.
- [30] Y. Kawamura, H. Mashiyama, K. Hasebe, J. Phys. Soc. Jpn. 71 (2002) 1694–1697.
- [31] T.J. Jacobsson, L.J. Schwan, M. Ottosson, A. Hagfeldt, T. Edvinsson, Inorg. Chem. 54 (2015) 10678–10685.
- [32] P.S. Whitefield, N. Herron, W.E. Guise, K. Page, Y.Q. Cheng, I. Milas, M.K. Crawford, Sci. Rep. 6 (2016) 35685.
- [33] P.S. Whitefield, N. Herron, W.E. Guise, K. Page, Y.Q. Cheng, I. Milas, M.K. Crawford, Sci. Rep. 7 (2016) 42831.
- [34] N.P. Bansal, R.H. Doremus, Handbook of Glass Properties, Academic Press, New York, NY, 1986.
- [35] W.C. Oliver, G.M. Pharr, J. Mater. Res. 7 (1992) 1564-1583.
- [36] B.R. Lawn, Fracture of Brittle Solids, Second Edition Cambridge University Press, Cambridge, U.K., 1993.
- [37] J.-J. Jang, G.M. Pharr, Acta Mater. 56 (2008) 4458–4469.
- [38] A. Poglitsch, D. Weber, J. Chem. Phys. 87 (1987) 6373–6378.
- [39] C.C. Stoumpos, C.D. Malliakas, M.G. Kanatzidis, Inorg. Chem. 52 (2013) 9019–9038.
- [40] D.G. Green, An Introduction to the Mechanical Properties of Ceramics, Cambridge University Press, Cambridge, UK, 1998.
- [41] L.B. Freund, S. Suresh, Thin Film Materials: Stess, Defect Formation and Surface Evolution, Cambridge University Press, Cambridge, UK, 2003.
- [42] H.H. Yu, M.Y. He, J.W. Hutchinson, Acta Mater. 49 (2001) 93-107.
- 43] Y. Zhou, M. Yang, W. Wu, A.L. Vasiliev, K. Zhu, N.P. Padture, J. Mater. Chem. A 3 (2015) 8178–8184.
- [44] Ž. Zhou, Z. Wang, Y. Zhou, S. Pang, D. Wang, H. Xu, Z. Liu, N.P. Padture, G. Cui, Angew. Chem. Int. Ed. 54 (2015) 9705–9709.
- [45] F. Ji, S. Pang, L. Zhang, Y. Zong, G. Cui, N.P. Padture, Y. Zhou, ACS Energy Lett. 2 (2017) 2727–2733.
- [46] N.J. Jeon, J.H. Noh, Y.C. Kim, W.S. Yang, S. Ryu, S.I. Seok, Nat. Mater. 9 (2014) 897–903.
- [47] B.D. Cullity, Elements of X-ray Diffraction, Second Edition Addison-Wesley, Boston, MA, 1978.
- 48] J. Zhao, Y. Deng, H. Wei, X. Zheng, Z. Yu, Y. Shao, J.E. Shield, J. Huang, Sci. Adv. 3 (2017) eaao5616.
- [49] M.E. Línes, A.M. Glass, Principles and Applications of Ferroelectrics and Related Materials, Clarendon Press, Oxford, UK, 1977.
- [50] M. Yang, Y. Zhou, Y. Zeng, C.-S. Jiang, N.P. Padture, K. Zhu, Adv. Mater. 27 (2015) 6363–6370.
- [51] I.A. Hermes, S.A. Bretschneider, V.W. Bergman, L.D.A. Klasen, J. Mars, W. Tremel, F. Laquai, H.-J. Butt, M. Mezger, R. Berger, B.J. Rodriguez, S.A.L. Weber, J. Phys. Chem. C 120 (2016) 5724–5731.
- [52] M.U. Rothman, W. Li, Y. Zhu, U. Bach, L. Spiccia, J. Etheridge, Y.-B. Cheng, Nat. Commun. 8 (2017) 14547.
- [53] E. Strelcov, Q. Dong, T. Li, J. Chae, Y. Shao, Y. Deng, A. Gruverman, J. Huang, A. Centrone, Sci. Adv. 3 (2017), e1602165.
- [54] C. Mercer, J.R. Williams, D.R. Clarke, A.G. Evans, Proc. Roy. Soc. A 463 (2007) 1393–1408.
- [55] N.P. Padture, Nat. Mater. 15 (2016) 804-809.
- [56] M.T. Weller, O.J. Weber, J.M. Frost, A. Walsh, J. Phys. Chem. Lett. 6 (2015) 3209–3212.
- [57] S. Sun, F.H. Isikgor, Z. Deng, F. Wei, G. Kieslich, P.D. Bristowe, J. Ouyang, A.K. Cheetham, SusChemSus 10 (2017) 3740–3745.
   [58] D.H. Fabini, C.C. Stoumpos, G. Laurita, A. Klttzoglou, A.G. Kontos, P. Falaras, M.G.
- Kanatzidis, R. Sheshadri, Angew. Chem. Int. Ed. 55 (2016) 15392–15396.
- [59] M.T. Weller, O.J. Weber, P.F. Henry, A.M.D. Pumpo, T.C. Hansen, Chem. Commun. 51 (2015) 4180–4183.
- [60] R. Cheacharon, N. Rolston, D. Harwood, K.A. Bush, R.H. Dauskardt, M.D. McGehee, Energy Environ. Sci. 11 (2018) 144–150.